AIMS Mathematics, 10(12): 29012–29036.
DOI: 10.3934/math.20251276
Received: 07 October 2025
Revised: 19 November 2025
Accepted: 25 November 2025
Published: 10 December 2025

https://www.aimspress.com/journal/Math

Research article

Williamson nanofluid flow and thermal transfer generated by a convectively heated stretched sheet via Fibonacci-Lucas polynomials

M. M. Khader[1], M. Adel[2,*], M. M. Babatin[1] and A. Alaidrous[3]

[1] Department of Mathematics and Statistics, College of Science, Imam Mohammad Ibn Saud Islamic University (IMSIU), Riyadh, Saudi Arabia

[2] Department of Mathematics, Faculty of Science, Islamic University of Madinah, Medina, Saudi Arabia

[3] Department of Mathematics, Faculty of Sciences, Umm Al-Qura University, Makkah, Saudi Arabia

* **Correspondence:** Email: adel@sci.cu.ed.eg.

Abstract: This work examined the two-dimensional, steady-state flow of a non-Newtonian nanofluid past an impermeable stretching sheet, incorporating temperature-dependent density, nonlinear rheology, nanoparticle transport mechanisms (thermophoresis/Brownian motion), and thermal radiation. The model was formed by nonlinear equations for mass, momentum, heat, and particle transport, and the surface heating condition was applied before using similarity transformations to reduce the system to ordinary differential equations. The numerical solution employs an innovative approach using merged Fibonacci-Lucas polynomials combined with least squares approximation, transforming the equations into algebraic form solved via the Newton iteration method. Rigorous convergence testing and error analysis verified the method's precision and reliability. The findings demonstrate that higher density and convection parameters substantially improve all transport processes, with heat transfer rates increasing by more than double. However, the Williamson parameter and Brownian motion show opposing influences, in which they decrease both surface friction and thermal transfer while simultaneously enhancing mass transport efficiency. Further, elevating the density parameter from 0.0 to 1.0 increases the skin-friction coefficient from 0.96084 to 1.18692 while simultaneously boosting both reduced Nusselt and Sherwood numbers. Conversely, augmenting the Williamson parameter from 0.0 to 0.6 reduces the skin-friction coefficient from 1.12885 to 0.96097, accompanied by moderate variations in heat and mass transfer rates. Extensive benchmarking against published numerical results demonstrated the scheme's accuracy, with close matching to existing solutions substantiating the reliability of our proposed approach.

Keywords: variable conductivity; mixed convection; thermal radiation; variable density; Williamson nanofluid; merged Fibonacci-Lucas polynomials; convergence analysis
Mathematics Subject Classification: 41A30, 65M60, 65N12, 76F12

Nomenclature

c	Constant (s^{-1})
D_B	Coefficient of Brownian diffusion ($\frac{m^2}{s}$)
q_r	Radiative heat flux ($\frac{W}{m^2}$)
c_p	Specific heat ($\frac{J}{kgK}$)
D_T	Coefficient of thermophoresis diffusion ($\frac{m^2}{s}$)
f	Dimensionless stream function
C	Concentration ($\frac{mol}{L}$)
T_f	Convection temperature (K)
C_w	Nanofluid concentration beside the sheet ($\frac{mol}{L}$)
u	Velocity component in the $x-$ direction ($\frac{m}{s}$)
v	Velocity component in the $y-$ direction ($\frac{m}{s}$)
S_c	Schmidt number
Cf_x	Local skin friction coefficient
T_∞	Ambient temperature (K)
Re_x	Local Reynolds number
Nu_x	Local Nusselt number
S_c	Schmidt number
Pr	Prandtl number
Sh_x	Local Sherwood number
x, y	Cartesian coordinates (m)

Greek symbols

τ	Heat capacity of nanoparticles in relation to the heat capacity of the basic fluid ($\frac{L}{mol}$)
ρ	Density of nanofluid ($\frac{kg}{m^3}$)
α	Thermal conductivity parameter
Ω_t	Thermophoresis parameter
ν	Kinematic viscosity ($\frac{m^2}{s}$)
Ω_b	Brownian motion parameter
κ_0	Thermal conductivity at the slit ($Wm^{-1}K^{-1}$)
Υ	Radiation parameter
κ	Thermal conductivity ($Wm^{-1}K^{-1}$)
λ	Williamson parameter
β	Convection parameter
η	Similarity variable
ϕ	Dimensionless concentration
δ	Density parameter
μ	Coefficient of viscosity ($kgm^{-1}s^{-1}$)
θ	Dimensionless temperature

1. Introduction

The development of nanoparticle-infused base fluids has transformed heat transfer solutions across multiple industries. These engineered suspensions demonstrate remarkable thermal properties,

including boosted conductivity and convection, that benefit applications from microelectronics cooling to large-scale solar thermal systems and specialized medical devices. The field of nanofluids originated with Choi's [1] groundbreaking demonstration of thermal conductivity enhancement through nanoparticle suspensions. This discovery sparked widespread investigation into nanofluid dynamics, heat transfer mechanisms, and industrial applications. Recent advances have significantly expanded our understanding of these complex fluids. Rashid et al. [2] demonstrated how nanoparticle morphology influences both entropy production and magnetohydrodynamic flow characteristics over stretched surfaces. Alali and Megahed [3] analyzed unsteady Casson nanofluid flow with velocity slip, quantifying the combined effects of viscous dissipation and thermal radiation. Abbas et al. [4] numerically simulated magnetized nanofluid flow past vertical cones, accounting for the transport of chemically reactive species. Garvandha et al. [5] investigated thermodynamic irreversibilities in inclined magnetic nanofluid flows along cylindrical geometries, while Amer et al. [6] addressed practical engineering scenarios by analyzing dissipative non-Newtonian nanofluid flow in porous media with surface roughness. Recent work has deepened our understanding of nanofluid behavior by exploring more intricate physical effects linked to modern thermal applications. Ali et al. [7] investigated how nanoparticle volume fraction dynamics, Coriolis forces, and magnetic fields influence entropy generation in mixed convection, offering deeper insight into thermodynamic irreversibility in rotating nanofluid environments. Meanwhile, Mishra and Pathak [8] analyzed the thermal-flow performance of an Ellis hybrid nanofluid containing polytetrafluoroethylene and single-walled carbon nanotubes over a stretching or shrinking cylinder, emphasizing the role of slip effects in enhancing heat-transfer behavior. Extending this direction, Mishra [9] further explored radiative Ellis hybrid nanofluid flow in a porous medium with slip, demonstrating how radiation and porosity modify the thermal response of hybrid suspensions. Collectively, these studies broaden the modeling framework of nanofluid transport and highlight the influence of multiphysics interactions on heat and momentum transfer. These investigations collectively highlight the necessity for advanced modeling approaches that accurately represent the coupled thermal, electromagnetic, and rheological behavior of nanofluids, a fundamental objective driving the current research.

The conventional assumption of fixed thermal conductivity proves inadequate for modeling advanced thermal-fluid systems, especially in high-temperature operations or nanofluid applications. Temperature-dependent thermal conductivity significantly enhances predictive accuracy in critical engineering domains including material thermal processing, microelectronics cooling, power generation systems, and industrial polymer manufacturing. This parameter's fundamental importance has driven numerous investigators to integrate variable thermal conductivity formulations into contemporary heat transfer models, substantially improving their physical fidelity and practical applicability. Several pivotal studies have demonstrated the importance of temperature-dependent thermal properties in fluid flow systems. Hamad et al. [10] examined radiative magnetohydrodynamic stagnation-point flow, showing that variable viscosity and thermal conductivity substantially alter flow behavior compared to constant-property assumptions. Khader and Megahed [11] analyzed porous media flows with varying sheet thickness and thermal conductivity, using differential transformation methods to quantify thermal boundary layer expansion. Further advancing this understanding, Hamid and Khan [12] established that thermal conductivity variations critically influence boundary layer evolution in unsteady Williamson nanofluid flows. Recent investigations by Jan et al. [13] on hybrid nanofluids revealed that thermal conductivity gradients enhance heat transfer sensitivity to surface

conditions. Khaleque et al. [14] extended this to power-law fluids, demonstrating coupled viscosity-thermal conductivity effects under radiative and diffusive transport. These pioneering studies directly informed our approach of incorporating thermal conductivity variations to authentically represent heat transfer dynamics in complex nanofluid systems experiencing coupled thermal and electromagnetic effects.

The role of temperature-dependent (variable) density is critically important in accurately capturing the physical behavior of complex fluid systems, especially in thermally driven processes such as material processing, lubrication, thermal management in electronics, and environmental heat transfer. In non-Newtonian nanofluid systems, where interactions between momentum, heat, and mass transfer are highly nonlinear, accounting for density variations, enhances model fidelity and enables realistic simulation of buoyancy-driven flows. Several investigations have addressed the significance of variable density in diverse thermal-fluid contexts. Previous research has extensively examined the influence of temperature-dependent density across various thermal-fluid scenarios. For instance, Salem et al. [15] investigated its effect on hydromagnetics mixed convection near moving plates, demonstrating its role in flow stratification. Siddiqa et al. [16] studied radiation-coupled mixed convection along permeable surfaces, emphasizing density-driven forces, while their later work [17] revealed thermal field sensitivity to density gradients in natural convection over horizontal disks. Recent advancements further highlight its importance: Ullah et al. [18] analyzed oscillatory heat transfer under reduced gravity and thermal stratification, and Ullah and his colleague [19] explored reactive nanofluid flows near magnetized sheets, with applications in machining and lubrication. Boukholda et al. [20] integrated thermal density effects in microelectronic cooling systems with magnetized nanofluids, and Haider et al. [21] examined viscous dissipation in magneto-Ree-Eyring nanofluids under slip conditions, reinforcing its impact on heat and mass transfer.

The proliferation of diverse numerical methodologies has fundamentally transformed scientific and engineering research. These evolving computational techniques provide robust solutions for analytically intractable problems, significantly expanding our capacity to model intricate physical systems. This advancement continues to drive innovation across multidisciplinary domains including thermal science, biomedical applications, materials engineering, and fluid mechanics, as example, Fahmy's research series ([22, 23]) has substantially progressed numerical methods in bioheat transfer. The initial work introduced a hybrid LRBFCM-GBEM algorithm for solving time-fractional dual-phase-lag bioheat transfer in functionally graded tissues. Subsequently, a nonlinear boundary-element formulation was developed to handle space-time fractional dual-phase-lag responses under electromagnetic heating. The third collaborative work further advanced boundary-element methods by incorporating memory effects through fractional bioheat modeling. Together, these contributions have significantly enriched numerical capabilities and expanded applications in biomedical thermal engineering.

The importance of the standard Fibonacci and Lucas polynomials (SFLPs), together with their generalized and modified sequences, has led to several research studies examining them. Theoretical findings on the SFLPs have been established. The authors in [24] have articulated conclusions on the SFLPs and their interrelations with other polynomials, especially orthogonal polynomials. Alternative formulations of Lucas polynomials were developed and utilized in [25] to tackle the time-fractional diffusion equation. Further contributions on these polynomials can be found in [26]. The studies are not restricted to the SFLPs, but many researchers are interested in introducing and investigating several

modified and generalized sequences of SFLPs. The authors in [27] have simplified certain radicals by utilizing two generalized categories of SFLPs. Generalized bivariate FLPs were examined [28]. In [29], the authors introduced and analyzed several k-Fibonacci and k-Lucas polynomial expressions. The generalizations of the FLPs were analyzed in [30]. Various sequences of the FLPs, together with their generalizations, have been employed in numerous studies to tackle different forms of differential equations. The authors of [31] have developed an approximate solution for a 2D problem utilizing a combination of FLPs. The researchers of [32] employed generalized Lucas polynomials and the wavelet approach to address some fractional optimal control problems.

While numerous studies ([33,34]) have explored nanofluid flow over stretching surfaces, none have simultaneously incorporated temperature-dependent viscosity, density variation, and linearly varying thermal conductivity within a second-grade fluid framework under convective heating. Moreover, the combined influence of these variable-property effects on the higher-order momentum formulation has not been quantified in prior literature. This study introduces a novel mathematical model that unifies these mechanisms and demonstrates, for the first time, their coupled impact on skin friction, heat transfer, and mass transport, thereby filling a clear gap in both theory and application.

2. Model development

This investigation examines a stable, 2D laminar flow of a non-Newtonian Williamson nanofluid past an impermeable stretching sheet. The base fluid demonstrates density variations with temperature and nonlinear viscous characteristics, while nanoparticles are subject to both thermophoresis and Brownian diffusion. The system incorporates thermal radiation effects and surface convective heat transfer. Below is the representation of the physical model.

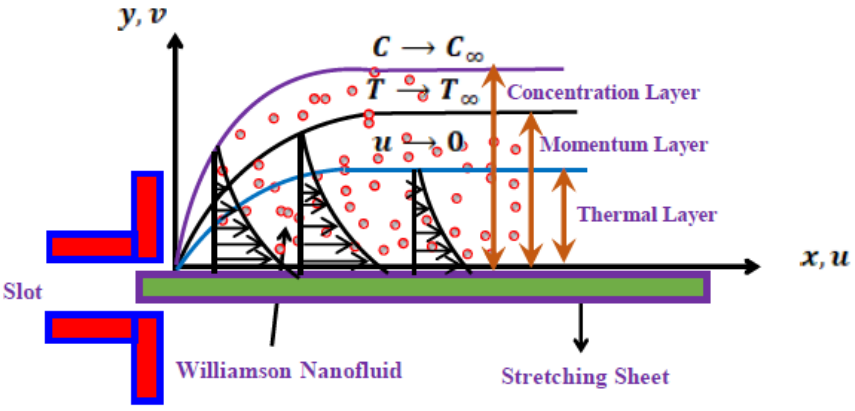

Figure 1. Model configuration.

The mathematical formulation employs continuity, momentum, energy, and mass conservation equations within the Boussinesq framework. The flow physics is captured through four governing equations:

Continuity Equation [15]:

$$\frac{\partial}{\partial x}(\rho\, u) + \frac{\partial}{\partial y}(\rho\, v) = 0. \tag{2.1}$$

Momentum Equation (non-Newtonian fluid model) [12]:

$$u\frac{\partial u}{\partial x} + v\frac{\partial u}{\partial y} = \frac{\mu}{\rho(T)}\frac{\partial}{\partial y}\left\{\left[1 + \frac{\Gamma}{\sqrt{2}}\left(\frac{\partial u}{\partial y}\right)\right]\left(\frac{\partial u}{\partial y}\right)\right\}. \tag{2.2}$$

Energy Equation (including thermophoresis, Brownian motion, and radiation) [12]:

$$u\frac{\partial T}{\partial x} + v\frac{\partial T}{\partial y} = \tau\left\{D_B\frac{\partial T}{\partial y}\frac{\partial C}{\partial y} + \frac{D_T}{T_\infty}\left(\frac{\partial T}{\partial y}\right)^2\right\} - \frac{1}{\rho(T)c_p}\left(\frac{\partial q_r}{\partial y}\right) + \frac{1}{\rho(T)c_p}\frac{\partial}{\partial y}\left(\kappa\frac{\partial T}{\partial y}\right). \tag{2.3}$$

Concentration Equation [12]:

$$u\frac{\partial C}{\partial x} + v\frac{\partial C}{\partial y} = \frac{D_T}{T_\infty}\frac{\partial^2 T}{\partial y^2} + D_B\frac{\partial^2 C}{\partial y^2}. \tag{2.4}$$

Here, we must observe that the governing equations represent the following physical principles: Eq (2.1) describes mass conservation with density variations; Eq (2.2) defines momentum balance for the non-Newtonian fluid with temperature-dependent viscosity and second-grade effects; Eq (2.3) expresses energy conservation incorporating Brownian motion, thermophoresis, radiation, and variable thermal conductivity; while Eq (2.4) governs nanoparticle concentration through diffusion and thermophoresis. This formulation ensures comprehensive physical representation of the complex transport phenomena. Now, the physical model requires satisfaction of these peripheral conditions:

$$u = cx, \qquad -\kappa\frac{\partial T}{\partial y} = h\left(T_f - T\right), \qquad C = C_w, \qquad v = 0, \qquad at \quad y = 0, \tag{2.5}$$

$$u \to 0, \qquad T \to T_\infty, \qquad C \to C_\infty, \qquad \text{as} \quad y \to \infty. \tag{2.6}$$

The nanoparticle concentration field is represented by C, where C_w indicates the wall concentration and C_∞ the free-stream value. Particle transport mechanisms include D_B (Brownian diffusion coefficient) for concentration-gradient driven motion and D_T (thermophoretic coefficient) for temperature-gradient migration. Thermal radiation is quantified by q_r, while κ denotes fluid thermal conductivity. The system's thermal properties are characterized by c_p (specific heat capacity) and τ (nanoparticle-to-fluid heat capacity ratio). The velocity field components u ($x-$direction) and v ($y-$direction) characterize the nanofluid motion. The formulation incorporates temperature-dependent density $\rho(T)$ to model thermal buoyancy effects. Fluid rheology is described by dynamic viscosity μ and non-Newtonian parameter Γ, which quantifies the nonlinear viscous response. Thermal conditions are specified through temperature variables: T (field), T_w (wall), T_f (surface convection), and T_∞ (ambient). Other relevant parameters include the stretching rate of the surface c, and the heat transfer coefficient at the wall h, while ν represents the kinematic viscosity of the fluid. Further, the radiative heat flux q_r in this study has been modeled strictly in accordance with the Rosseland diffusion approximation [35]. The formulation used follows the standard assumptions of optically thick media, where the radiative contribution is represented as a diffusion process. The linearization of the radiative

term and its incorporation into the energy equation fully adhere to the classical Rosseland framework widely adopted in thermal boundary-layer analysis. To reduce the system, the following similarity transformations are introduced:

$$\theta(\eta) = \frac{T_\infty - T}{T_\infty - T_w}, \qquad \Psi = \sqrt{c\,\nu}\, x\, f(\eta), \qquad u = \frac{1}{\rho}\frac{\partial \Psi}{\partial y}, \qquad v = -\frac{1}{\rho}\frac{\partial \Psi}{\partial x}, \tag{2.7}$$

$$\phi(\eta) = \frac{C_\infty - C}{C_\infty - C_w}, \qquad \eta = \sqrt{c}\nu \int_0^y \rho(y)\, dy. \tag{2.8}$$

To simplify the governing system, the stream function Ψ is introduced such that it automatically satisfies the continuity equation. The similarity variable η reduces the partial differential equations to ordinary ones, the dimensionless concentration is given by $\phi(\eta)$, and the dimensionless temperature is given by $\theta(\eta)$. The function $f(\eta)$ emerges from the similarity transformation of the stream function. The formulation considers thermally induced changes in the Williamson fluid's density and viscosity characteristics during motion, as quantified through the following mathematical expressions ([36,37]):

$$\rho(T) = \rho_0 e^{-\delta\,\theta}, \qquad \kappa = \kappa_0\,(1 + \alpha\,\theta)\,, \tag{2.9}$$

where ρ_0 is the constant density, κ_0 is the constant conductivity, δ is the density parameter, and α is the conductivity factor. By computing the required differential terms and implementing suitable transformations (2.7) and (2.8) for the model (2.2) to (2.4), the mass conservation condition is satisfied. We subsequently obtain the complete system of transport equations for concentration, thermal energy, and fluid momentum, shown below:

$$(f''' - \delta\,\theta'\,f'')\left(\lambda\, f'' + e^{\delta\,\theta}\right) + e^{2\delta\,\theta}\left(f f'' - f'^{\,2}\right) = 0, \tag{2.10}$$

$$\frac{1}{\Pr}\left\{\left(\theta'' - \delta\theta'^{\,2}\right)(1 + \alpha\,\theta + \Upsilon) - \alpha\,\theta'^{\,2}\right\} e^{\delta\,\theta} + e^{2\,\delta\,\theta} f\,\theta' + \Omega_b \phi'\theta' + \Omega_t \theta'^2 = 0, \tag{2.11}$$

$$\phi'' - \delta\,\theta'\phi' + \frac{\Omega_t}{\Omega_b}\left(\theta'' - \delta\,\theta'^{\,2}\right) + S_c\, f\phi'\, e^{2\,\delta\,\theta} = 0. \tag{2.12}$$

The presented terms below result from carefully executed simplifications of the original framework conditions documented in the referenced Eqs (2.5) and (2.6):

$$f = 0, \qquad f' = 1, \qquad \theta' = -\beta\,(1 - \theta), \qquad \phi = 1, \qquad at \quad \eta = 0, \tag{2.13}$$

$$f' \to 0, \qquad \theta \to 0, \qquad \phi \to 0, \qquad \text{as} \quad \eta \to \infty. \tag{2.14}$$

The dynamics of this complex system are dictated by a particular combination of influential variables that capture the essential physics. We formally identify these controlling parameters through the following definitions:

$$\lambda = \sqrt{\frac{2\,c}{\nu}}\, u_w\, \Gamma, \qquad \Upsilon = \frac{16\sigma^* T_\infty^3}{3\,\kappa_0\, k^*}, \qquad \Omega_t = \frac{\tau \rho_0 D_T\,(T_w - T_\infty)}{\mu_0 T_\infty}, \qquad \beta = \frac{h}{\kappa_0}\sqrt{\frac{\mu_0}{c\,\rho_0}}, \tag{2.15}$$

$$\Pr = \frac{\mu\, c_p}{\kappa_0}, \qquad \Omega_b = \frac{\tau \rho_0 D_B\,(C_w - C_\infty)}{\mu}, \qquad S_c = \frac{\mu}{\rho_0 D_B}. \tag{2.16}$$

In this study, the parameter λ represents a local Williamson parameter based on the $x-$coordinate. As a spatially dependent variable, its value evolves throughout the flow field, establishing the validity of the solution strictly within a local similarity framework. For graphical representation, specific constant values of λ were selected, corresponding to flow analysis at fixed $x-$positions across all $y-$coordinates. The definitions of these factors are: local Williamson parameter λ, radiation parameter Υ, thermophoresis parameter Ω_t, convection parameter β, Prandtl number Pr, Brownian motion parameter Ω_b, and Schmidt number S_c. Further, this study examines several key engineering parameters that characterize the transport phenomena at the surface: the modified skin friction coefficient $Cf_xRe^{\frac{1}{2}}$, which quantifies shear stress effects; the scaled local Nusselt number $Nu_xRe^{\frac{-1}{2}}$, representing heat transfer efficiency; and the dimensionless Sherwood number $Sh_xRe^{\frac{-1}{2}}$, describing mass transfer rates. These parameters serve as critical indicators of system performance and can be mathematically defined through the following relationships:

$$\frac{1}{2}Cf_xRe^{\frac{1}{2}} = -e^{-\delta\theta(0)}\left(e^{\delta\theta(0)} + \frac{\lambda}{2}f''(0)\right)f''(0), \qquad Sh_xRe^{\frac{-1}{2}} = -\phi'(0), \tag{2.17}$$

$$Nu_xRe^{\frac{-1}{2}} = -(1 + \Upsilon + \alpha\theta(0))\theta'(0). \tag{2.18}$$

3. Implementation of the approximation method

This work aims to investigate the combined Fibonacci-Lucas polynomials and their characteristics. Furthermore, we provide an approximation formula for the derivatives of the MFLPs. Then, we will use it for solving the proposed model with the help of the least squares method.

3.1. Fundamentals of FLPs

We can derive the SFLPs using the following two recurrence formulas, respectively [38]:

$$\begin{aligned} &F_i(z) - zF_{i-1}(z) - F_{i-2}(z) = 0, \qquad F_0(z) = 0, \qquad F_1(z) = 1, \\ &L_i(z) - zL_{i-1}(z) - L_{i-2}(z) = 0, \qquad L_0(z) = 2, \qquad L_1(z) = z. \end{aligned} \tag{3.1}$$

The Fibonacci and Lucas polynomials can be represented by [38]:

$$\begin{aligned} F_m(z) &= \sum_{k=0}^{\lfloor\frac{m-1}{2}\rfloor}\binom{m-k}{k}z^{m-2k-1}, \\ L_m(z) &= \sum_{s=0}^{\lfloor\frac{m}{2}\rfloor}\frac{m}{m-k}\binom{m-k}{k}z^{m-2k}. \end{aligned} \tag{3.2}$$

Also, we present two categories of non-orthogonal polynomials: the generalized Fibonacci polynomials $F_r^{A,B}(z)$, and the generalized Lucas polynomials $L_r^{\bar{A},\bar{B}}(z)$, both of which were examined in [27], and can be expressed, respectively, as follows:

$$\begin{aligned} &F_r^{A,B}(z) = AzF_{r-1}^{A,B}(z) + BF_{r-2}^{A,B}(z), \quad F_0^{A,B}(z) = 1, \quad F_1^{A,B}(z) = Az, \quad r \geq 2, \\ &L_r^{\bar{A},\bar{B}}(z) = \bar{A}zL_{r-1}^{\bar{A},\bar{B}}(z) + \bar{B}L_{r-2}^{\bar{A},\bar{B}}(z), \quad L_0^{\bar{A},\bar{B}}(z) = 2, \quad L_1^{\bar{A},\bar{B}}(z) = \bar{A}z, \quad r \geq 2. \end{aligned} \tag{3.3}$$

3.2. Presenting the merged FLPs

This subsection introduces a new merged FLP and gives some characteristics of these polynomials.

The two recursive formulas in (3.1) show that both FLPs adhere to the same pattern; however, they commence with distinct initial values; therefore, we can get [39]:

$$\phi_i(z) - z\phi_{i-1}(z) - \phi_{i-2}(z) = 0, \qquad \phi_0(z) = a, \qquad \phi_1(z) = bz, \tag{3.4}$$

generalizes the two sets in (3.1). We symbolize $\phi_i(z) = FL_i^{a,b}(z)$ for the merged Fibonacci and Lucas polynomials, that is:

$$FL_i^{a,b}(z) - zFL_{i-1}^{a,b}(z) - FL_{i-2}^{a,b}(z) = 0, \qquad FL_0^{a,b}(z) = a, \qquad FL_1^{a,b}(z) = bz. \tag{3.5}$$

Both $F_i(z)$ and $L_i(z)$ are particular polynomials of $FL_i^{a,b}(z)$. In fact, we have

$$F_{i+1}(z) = FL_i^{1,1}(z), \qquad L_i(z) = FL_i^{2,1}(z). \tag{3.6}$$

Remark 3.1. *[39]*

The fundamental concept for deriving the formulae associated with the polynomials $FL_i^{a,b}(z)$ that fulfil (3.5) is encapsulated in the following theorem, which demonstrates that $FL_i^{a,b}(z)$ can be articulated in terms of two specific Fibonacci polynomials.

Theorem 3.1. *[39]*

The MFLPs of order $\ell \in \mathbb{Z}^+$ can be expressed as:

$$FL_\ell^{a,b}(z) = b\,F_{\ell+1}(z) + (a-b)\,F_{\ell-1}(z). \tag{3.7}$$

Theorem 3.2.

Consider a positive integer i. The power of impersonation of $FL_i^{a,b}(z)$ is:

$$FL_i^{a,b}(z) = \sum_{k=0}^{\lfloor \frac{i}{2} \rfloor} \frac{(i-2k+1)_{k-1}((i-2k)b + ka)}{k!}\, z^{i-2k}. \tag{3.8}$$

3.3. A derivative expression of the MFLPs

In this subsection, we give an expression for the derivatives of the MFLPs in terms of other parameters of the MFLPs. From this expression, some important specific formulas are obtained.

Theorem 3.3. *[39]*

Consider the two positive integers s and m with $m \geq s$. $D^s FL_m^{a,b}(z)$ has the following expression:

$$\begin{aligned} D^s FL_m^{a,b}(z) = \frac{1}{a} \sum_{p=0}^{m-s} \frac{(-1)^p (s+1)_{p-1}(m-p-1)!}{p!(-p+m-s)!} \cdot \\ (-2bp(p+s) + ap(-m+p+s) + bm(2p+s)) FL_{m-s-2p}^{a,b}(z). \end{aligned} \tag{3.9}$$

As a special case, the derivatives $D^2\, FL_m^{a,b}(z)$ can be expressed as combinations of their original ones.

Any function $\psi(z)$ can be approximated in terms of the MFLPs as follows:

$$\psi(z) \simeq \psi_m(z) = \sum_{\ell=0}^{m} c_\ell\, FL_\ell^{a,b}(z). \tag{3.10}$$

3.4. Approximate formula of the derivatives

The essential objective of this part is to give an approximate formula for the derivatives of the MFLPs. We will commence with the presentation of the subsequent lemma.

Lemma 3.1.

Let $FL_{\ell}^{a,b}(z)$ be an MFLP for $\ell = 0, 1, \ldots, n-1$, where $n > 0$. Then

$$D^{(n)}\, FL_{\ell}^{a,b}(z) = 0. \tag{3.11}$$

Proof. This lemma can be proved by using equation (3.8) and the properties of the differential operator. □

Theorem 3.4.

Suppose that the function $\psi(z)$ is approximated as in (3.10), and then $D^{(n)}(\psi_m(z))$ can be given as:

$$D^{(n)}(\psi_m(z)) = \sum_{\ell=n}^{m} \sum_{i=n}^{\lfloor \frac{\ell}{2} \rfloor} c_\ell\, \Phi_{i,\ell,n}^{a,b}\, z^{\ell-2i-n}, \qquad \Phi_{i,\ell,n}^{a,b} = \frac{(\ell-2i+1)_{i-1}((\ell-2\,i)b+ia)(\ell-2i)_n}{i!}. \tag{3.12}$$

Proof. Having the analytic expression of the MFLPs, using characteristics of $D^{(n)}$, and with the help of Lemma 1, one gets for $i = n, n+1, ..., m$:

$$\begin{aligned} D^{(n)}(\psi_m(z)) &= D^{(n)}\left[\sum_{\ell=0}^{m} c_\ell\, FL_{\ell}^{a,b}(z)\right] = D^{(n)}\left[\sum_{\ell=0}^{m} c_\ell \sum_{i=0}^{\lfloor \frac{\ell}{2} \rfloor} \frac{(\ell-2i+1)_{i-1}((\ell-2\,i)b+ia)}{i!}\, z^{\ell-2i}\right] \\ &= \sum_{\ell=0}^{m} \sum_{i=0}^{\lfloor \frac{\ell}{2} \rfloor} c_\ell \frac{(\ell-2i+1)_{i-1}((\ell-2\,i)b+ia)}{i!}\, D^{(n)}\, z^{\ell-2i} \\ &= \sum_{\ell=n}^{m} \sum_{i=n}^{\lfloor \frac{\ell}{2} \rfloor} c_\ell \frac{(\ell-2i+1)_{i-1}((\ell-2\,i)b+ia)(\ell-2i)_n}{i!}\, z^{\ell-2i-n} \\ &= \sum_{\ell=n}^{m} \sum_{i=n}^{\lfloor \frac{\ell}{2} \rfloor} c_\ell\, \Phi_{i,\ell,n}^{a,b}\, z^{\ell-2i-n}, \end{aligned} \tag{3.13}$$

where $\Phi_{i,\ell,n}^{a,b}$ is defined in (3.12), and this concludes the proof of the theorem. □

Now, we examine the convergence analysis of the approach suggested in this study. We shall present the subsequent theorem.

Theorem 3.5.

Assume that $D^{(j\,n)}\psi(z) \in C(0,1)$ for $j = 0, 1, \ldots, m$ and $\bar{\Psi}_m = \text{span}\left\{FL_{\ell}^{a,b}(z)\right\}_{\ell=0}^{m}$. If $\psi_m(z)$ defined in (3.10) is the best approximation (BA) to $\psi(z)$ from $\bar{\Psi}_m$ and:

$$\mathbb{S}_m(\psi(z)) = \int_0^1 \left[\psi(z) - \psi_m(z)\right]^2 dz,$$

then

$$\lim_{m\to\infty} \mathbb{S}_m(\psi(z)) = 0.$$

Proof. First, we can take into consideration the following generalized Taylor formula:

$$\psi^*(z) = \sum_{\ell=0}^{m} \frac{z^{\ell n}}{(\ell\, n)!} D^{(\ell\, n)} \psi\,(0^+)\,.$$

It is readily seen from formula (3.14) and $\psi^*(z) \in \bar{\Psi}_m$ that one gets

$$|\psi(z) - \psi^*(z)| < \frac{z^{(m+1)n}}{((m+1)n)!}\Delta_n,$$

where $\Delta_n \geq \sup_{\xi\in(0,1]} \left|D^{(mn+n)}\psi(\xi)\right|$. On account of this, $\psi_m(z)$ is the BA of $\psi(z)$, and due to the above relation, one can conclude:

$$\begin{aligned} \|\psi(z) - \psi_m(z)\|_2^2 \leq \|\psi(z) - \psi^*(z)\|_2^2 &= \int_0^1 |\psi(z) - \psi^*(z)|^2 dz \\ &\leq \int_0^1 \Delta_n^2 \frac{z^{(2m+2)n}}{((mn+n)!)^2} dz \\ &= \frac{\Delta_n^2}{((mn+n)!)^2} \int_0^1 z^{(2m+2)n} dz \\ &= \frac{\Delta_n^2}{((mn+n)!)^2((2m+2)n+1)}. \end{aligned} \tag{3.14}$$

Consequently, one can get $\lim_{m\to\infty} \|\psi(z) - \psi_m(z)\|_2^2 = 0$. □

4. Numerical enforcement of the MFLPs

To employ the MFLPs and obtain the required scheme for solving (2.10)–(2.14) inside the domain $[0, \eta_\infty] = [0, 6]$, we follow the following steps (algorithm):

(1) We approximate $f(\eta)$, $\theta(\eta)$, and $\phi(\eta)$ by $f_m(\eta)$, $\theta_m(\eta)$, and $\phi_m(\eta)$ in the following form:

$$f_m(\eta) = \sum_{k=0}^{m} c_k FL_k^{a,b}(\eta), \qquad \theta_m(\eta) = \sum_{k=0}^{m} d_k\, FL_k^{a,b}(\eta), \qquad \phi_m(\eta) = \sum_{k=0}^{m} e_k\, FL_k^{a,b}(\eta). \tag{4.1}$$

(2) By substituting from Eqs (3.12) and (4.1) in (2.10)–(2.14), we obtain:

$$\begin{aligned} &\left(\sum_{\ell=3}^{m}\sum_{i=3}^{\lfloor\frac{\ell}{2}\rfloor} c_\ell\, \Phi_{i,\ell,3}^{a,b}\, \eta^{\ell-2i-3} - \delta \left(\sum_{\ell=2}^{m}\sum_{i=2}^{\lfloor\frac{\ell}{2}\rfloor} c_\ell\, \Phi_{i,\ell,2}^{a,b}\, \eta^{\ell-2i-2}\right)\left(\sum_{\ell=1}^{m}\sum_{i=1}^{\lfloor\frac{\ell}{2}\rfloor} d_\ell\, \Phi_{i,\ell,1}^{a,b}\, \eta^{\ell-2i-1}\right)\right). \\ &\left(\lambda \sum_{\ell=2}^{m}\sum_{i=2}^{\lfloor\frac{\ell}{2}\rfloor} c_\ell\, \Phi_{i,\ell,2}^{a,b}\, \eta^{\ell-2i-2} + Exp\left[\delta \sum_{k=0}^{m} d_k\, FL_k^{a,b}(\eta)\right]\right) + Exp\left[2\delta \sum_{k=0}^{m} d_k\, FL_k^{a,b}(\eta)\right]. \\ &\left(\left(\sum_{k=0}^{m} c_k\, FL_k^{a,b}(\eta)\right)\left(\sum_{\ell=2}^{m}\sum_{i=2}^{\lfloor\frac{\ell}{2}\rfloor} c_\ell\, \Phi_{i,\ell,2}^{a,b}\, \eta^{\ell-2i-2}\right) - \left(\sum_{\ell=1}^{m}\sum_{i=1}^{\lfloor\frac{\ell}{2}\rfloor} c_\ell\, \Phi_{i,\ell,1}^{a,b}\, \eta^{\ell-2i-1}\right)^2\right) = 0, \end{aligned} \tag{4.2}$$

$$\frac{1}{\mathrm{Pr}}\Bigg[\left(\sum_{\ell=2}^{m}\sum_{i=2}^{\lfloor\frac{\ell}{2}\rfloor} d_\ell\,\Phi_{i,\ell,2}^{a,b}\,\eta^{\ell-2i-2} - \delta\left(\sum_{\ell=1}^{m}\sum_{i=1}^{\lfloor\frac{\ell}{2}\rfloor} d_\ell\,\Phi_{i,\ell,1}^{a,b}\,\eta^{\ell-2i-1}\right)^2\right)\cdot$$
$$\left(1+\Upsilon+\alpha\sum_{k=0}^{m} d_k\,FL_k^{a,b}(\eta)\right) - \alpha\left(\sum_{\ell=1}^{m}\sum_{i=1}^{\lfloor\frac{\ell}{2}\rfloor} d_\ell\,\Phi_{i,\ell,1}^{a,b}\,\eta^{\ell-2i-1}\right)^2\Bigg]\cdot$$
$$Exp\left[\delta\sum_{k=0}^{m} d_k\,FL_k^{a,b}(\eta)\right] + Exp\left[2\,\delta\sum_{k=0}^{m} d_k\,FL_k^{a,b}(\eta)\right]\left(\sum_{k=0}^{m} c_k\,FL_k^{a,b}(\eta)\right)\cdot \tag{4.3}$$
$$\left(\sum_{\ell=1}^{m}\sum_{i=1}^{\lfloor\frac{\ell}{2}\rfloor} d_\ell\,\Phi_{i,\ell,1}^{a,b}\,\eta^{\ell-2i-1}\right) + \Omega_b\left(\sum_{\ell=1}^{m}\sum_{i=1}^{\lfloor\frac{\ell}{2}\rfloor} d_\ell\,\Phi_{i,\ell,1}^{a,b}\,\eta^{\ell-2i-1}\right)\left(\sum_{\ell=1}^{m}\sum_{i=1}^{\lfloor\frac{\ell}{2}\rfloor} e_\ell\,\Phi_{i,\ell,1}^{a,b}\,\eta^{\ell-2i-1}\right)$$
$$+\,\Omega_t\left(\sum_{\ell=1}^{m}\sum_{i=1}^{\lfloor\frac{\ell}{2}\rfloor} d_\ell\,\Phi_{i,\ell,1}^{a,b}\,\eta^{\ell-2i-1}\right)^2 = 0,$$

$$\sum_{\ell=2}^{m}\sum_{i=2}^{\lfloor\frac{\ell}{2}\rfloor} e_\ell\,\Phi_{i,\ell,2}^{a,b}\,\eta^{\ell-2i-2} - \delta\left(\sum_{\ell=1}^{m}\sum_{i=1}^{\lfloor\frac{\ell}{2}\rfloor} d_\ell\,\Phi_{i,\ell,1}^{a,b}\,\eta^{\ell-2i-1}\right)\left(\sum_{\ell=1}^{m}\sum_{i=1}^{\lfloor\frac{\ell}{2}\rfloor} e_\ell\,\Phi_{i,\ell,1}^{a,b}\,\eta^{\ell-2i-1}\right)$$
$$+\frac{\Omega_t}{\Omega_b}\left(\sum_{\ell=2}^{m}\sum_{i=2}^{\lfloor\frac{\ell}{2}\rfloor} d_\ell\,\Phi_{i,\ell,2}^{a,b}\,\eta^{\ell-2i-2} - \delta\left(\sum_{\ell=1}^{m}\sum_{i=1}^{\lfloor\frac{\ell}{2}\rfloor} d_\ell\,\Phi_{i,\ell,1}^{a,b}\,\eta^{\ell-2i-1}\right)^2\right) \tag{4.4}$$
$$+\,S_c\left(\sum_{k=0}^{m} c_k\,FL_k^{a,b}(\eta)\right)\left(\sum_{\ell=1}^{m}\sum_{i=1}^{\lfloor\frac{\ell}{2}\rfloor} e_\ell\,\Phi_{i,\ell,1}^{a,b}\,\eta^{\ell-2i-1}\right)Exp\left[2\,\delta\sum_{k=0}^{m} d_k\,FL_k^{a,b}(\eta)\right] = 0,$$

$$\sum_{k=0}^{m} c_k\,FL_k^{a,b}(0) = 0, \qquad \sum_{k=0}^{m} c_k\,D^{(1)}FL_k^{a,b}(0) = 1, \qquad \sum_{k=0}^{m} e_k\,FL_k^{a,b}(0) = 1,$$
$$\sum_{k=0}^{m} d_k\,D^{(1)}FL_k^{a,b}(0) + \beta\left(1-\sum_{k=0}^{m} d_k\,FL_k^{a,b}(0)\right) = 0, \tag{4.5}$$
$$\sum_{k=0}^{m} c_k\,D^{(1)}FL_k^{a,b}(\eta_\infty) = 0, \qquad \sum_{k=0}^{m} d_k\,FL_k^{a,b}(\eta_\infty) = 0, \qquad \sum_{k=0}^{m} e_k\,FL_k^{a,b}(\eta_\infty) = 0.$$

(3) To conduct a comprehensive numerical analysis through simulation, we assume that the numerical solution $(f_m(\eta),\ \theta_m(\eta),\ \phi_m(\eta))$ for the presented issue may be provided. Consequently, we estimate the residual error function (REF) as follows:

$$
\begin{aligned}
&\mathrm{REF}_1(\eta;a,b,m) = \Big[\sum_{\ell=3}^{m}\sum_{i=3}^{\lfloor\frac{\ell}{2}\rfloor} c_\ell\,\Phi_{i,\ell,3}^{a,b}\,\eta^{\ell-2i-3} - \delta\left(\sum_{\ell=2}^{m}\sum_{i=2}^{\lfloor\frac{\ell}{2}\rfloor} c_\ell\,\Phi_{i,\ell,2}^{a,b}\,\eta^{\ell-2i-2}\right)\Big]\cdot\\
&\left(\sum_{\ell=1}^{m}\sum_{i=1}^{\lfloor\frac{\ell}{2}\rfloor} d_\ell\,\Phi_{i,\ell,1}^{a,b}\,\eta^{\ell-2i-1}\right)\Big]\left(\lambda\sum_{\ell=2}^{m}\sum_{i=2}^{\lfloor\frac{\ell}{2}\rfloor} c_\ell\,\Phi_{i,\ell,2}^{a,b}\,\eta^{\ell-2i-2} + Exp\left[\delta\sum_{k=0}^{m} d_k\,FL_k^{a,b}(\eta)\right]\right)\\
&+ Exp\left[2\delta\sum_{k=0}^{m} d_k\,FL_k^{a,b}(\eta)\right]\Big(\left(\sum_{k=0}^{m} c_k\,FL_k^{a,b}(\eta)\right)\left(\sum_{\ell=2}^{m}\sum_{i=2}^{\lfloor\frac{\ell}{2}\rfloor} c_\ell\,\Phi_{i,\ell,2}^{a,b}\,\eta^{\ell-2i-2}\right)\\
&-\left(\sum_{\ell=1}^{m}\sum_{i=1}^{\lfloor\frac{\ell}{2}\rfloor} c_\ell\,\Phi_{i,\ell,1}^{a,b}\,\eta^{\ell-2i-1}\right)^2\Big) \simeq 0,
\end{aligned}
\tag{4.6}
$$

$$
\begin{aligned}
&\mathrm{REF}_2(\eta;a,b,m) = \frac{1}{\mathrm{Pr}}\Big[\left(\sum_{\ell=2}^{m}\sum_{i=2}^{\lfloor\frac{\ell}{2}\rfloor} d_\ell\,\Phi_{i,\ell,2}^{a,b}\,\eta^{\ell-2i-2} - \delta\left(\sum_{\ell=1}^{m}\sum_{i=1}^{\lfloor\frac{\ell}{2}\rfloor} d_\ell\,\Phi_{i,\ell,1}^{a,b}\,\eta^{\ell-2i-1}\right)^2\right)\cdot\\
&\left(1+\Upsilon+\alpha\sum_{k=0}^{m} d_k\,FL_k^{a,b}(\eta)\right) - \alpha\left(\sum_{\ell=1}^{m}\sum_{i=1}^{\lfloor\frac{\ell}{2}\rfloor} d_\ell\,\Phi_{i,\ell,1}^{a,b}\,\eta^{\ell-2i-1}\right)^2\Big]\cdot\\
&Exp\left[\delta\sum_{k=0}^{m} d_k\,FL_k^{a,b}(\eta)\right] + Exp\left[2\,\delta\sum_{k=0}^{m} d_k\,FL_k^{a,b}(\eta)\right]\left(\sum_{k=0}^{m} c_k\,FL_k^{a,b}(\eta)\right)\cdot\\
&\left(\sum_{\ell=1}^{m}\sum_{i=1}^{\lfloor\frac{\ell}{2}\rfloor} d_\ell\,\Phi_{i,\ell,1}^{a,b}\,\eta^{\ell-2i-1}\right) + \Omega_b\left(\sum_{\ell=1}^{m}\sum_{i=1}^{\lfloor\frac{\ell}{2}\rfloor} d_\ell\,\Phi_{i,\ell,1}^{a,b}\,\eta^{\ell-2i-1}\right)\left(\sum_{\ell=1}^{m}\sum_{i=1}^{\lfloor\frac{\ell}{2}\rfloor} e_\ell\,\Phi_{i,\ell,1}^{a,b}\,\eta^{\ell-2i-1}\right)\\
&+\Omega_t\left(\sum_{\ell=1}^{m}\sum_{i=1}^{\lfloor\frac{\ell}{2}\rfloor} d_\ell\,\Phi_{i,\ell,1}^{a,b}\,\eta^{\ell-2i-1}\right)^2 \simeq 0,
\end{aligned}
\tag{4.7}
$$

$$
\begin{aligned}
&\mathrm{REF}_3(\eta;a,b,m) = \sum_{\ell=2}^{m}\sum_{i=2}^{\lfloor\frac{\ell}{2}\rfloor} e_\ell\,\Phi_{i,\ell,2}^{a,b}\,\eta^{\ell-2i-2} - \delta\left(\sum_{\ell=1}^{m}\sum_{i=1}^{\lfloor\frac{\ell}{2}\rfloor} d_\ell\,\Phi_{i,\ell,1}^{a,b}\,\eta^{\ell-2i-1}\right)\cdot\\
&\left(\sum_{\ell=1}^{m}\sum_{i=1}^{\lfloor\frac{\ell}{2}\rfloor} e_\ell\,\Phi_{i,\ell,1}^{a,b}\,\eta^{\ell-2i-1}\right) + \frac{\Omega_t}{\Omega_b}\left(\sum_{\ell=2}^{m}\sum_{i=2}^{\lfloor\frac{\ell}{2}\rfloor} d_\ell\,\Phi_{i,\ell,2}^{a,b}\,\eta^{\ell-2i-2} - \delta\left(\sum_{\ell=1}^{m}\sum_{i=1}^{\lfloor\frac{\ell}{2}\rfloor} d_\ell\,\Phi_{i,\ell,1}^{a,b}\,\eta^{\ell-2i-1}\right)^2\right)\\
&+S_c\left(\sum_{k=0}^{m} c_k\,FL_k^{a,b}(\eta)\right)\left(\sum_{\ell=1}^{m}\sum_{i=1}^{\lfloor\frac{\ell}{2}\rfloor} e_\ell\,\Phi_{i,\ell,1}^{a,b}\,\eta^{\ell-2i-1}\right)Exp\left[2\,\delta\sum_{k=0}^{m} d_k\,FL_k^{a,b}(\eta)\right] \simeq 0.
\end{aligned}
\tag{4.8}
$$

The minimal residual ($\mathrm{REF}_i(\eta;a,b,m)\to 0,\ i=1,2,3$) indicates that the approximate solution closely aligns with the exact solution, meaning the absolute error approaches zero. This kind of error is used when the true solution is unknown, which is sometimes difficult in the case of highly nonlinear differential equations. Ultimately, the REF possesses various other forms; for further details, refer to [40].

(4) By applying the least squares method, we define the following objective functions:

$$\begin{aligned} SF_1[c_0, c_1, ..., c_m] &= \int_0^3 [\mathrm{REF}_1(\eta; a, b, m)]\, d\eta, \\ SF_2[d_0, d_1, ..., d_m] &= \int_0^3 [\mathrm{REF}_2(\eta; a, b, m)]\, d\eta, \\ SF_3[e_0, e_1, ..., e_m] &= \int_0^3 [\mathrm{REF}_3(\eta; a, b, m)]\, d\eta. \end{aligned} \tag{4.9}$$

To minimize $SF_1[c_0, c_1, ..., c_m]$, $SF_2[d_0, d_1, ..., d_m]$, $SF_3[e_0, e_1, ..., e_m]$, and obtain the optimal values of c_i, d_i, e_i, $i = 0, 1, 2, ..., m$, we construct the following relations:

$$\frac{\partial SF_1}{\partial c_k} = 0, \qquad \frac{\partial SF_2}{\partial d_k} = 0, \qquad \frac{\partial SF_3}{\partial e_k} = 0, \qquad k = 0, 1, 2, ..., m. \tag{4.10}$$

(5) Equations (4.10) constitute a set of $(3m + 3)$ nonlinear algebraic equations that can be resolved utilizing the Newton iteration approach to get the coefficients $\{c_k,\ d_k,\ e_k\}_{k=0}^{m}$. Furthermore, we may ascertain the numerical solution of the model (2.10)–(2.14) utilizing the formulas (4.1).

5. Validation of the numerical scheme

The current model's credibility was established through systematic comparison with the benchmark study of Nadeem et al. [41], who investigated pseudoplastic Williamson fluid flow over a stretching surface. Their analytical approach utilized similarity transformations and boundary layer theory, with solutions obtained via homotopy analysis. Significantly, their formulation represents a specific instance of our comprehensive model when the non-Newtonian Williamson parameter δ assumes a zero value. Tabulated results (Table 1) reveal remarkable consistency between both studies, with marginal deviations not exceeding 0.0002%. This quantitative agreement rigorously validates our generalized methodology's mathematical soundness and computational precision, while demonstrating its backward compatibility with established solutions under limiting conditions.

Table 1. Numerical values of $\frac{1}{2}Cf_xRe^{\frac{1}{2}}$ for distinct values of λ at $\delta = 0.0$.

λ	Nadeem et al. [41]	Present work
0.0	1.000000	1.00000000000
0.1	0.976588	0.97658778901
0.2	0.939817	0.93981659028
0.3	0.882720	0.88271899807

Further, Table 2 presents another validation of the present numerical scheme by comparing the computed values of the reduced Nusselt number in terms of $(-\theta'(0))$, with the benchmark results reported by Khan and Pop [42] for a wide range of Prandtl numbers with the condition $(\theta(0) = 1)$. As the table shows, the values obtained in this study match the reference data with excellent accuracy across all tested cases–from low-Prandtl-number fluids (Pr = 0.07) to highly viscous thermal regimes

(Pr = 7.0). The close agreement, often to more than six significant figures, confirms the robustness and reliability of the current computational formulation and its consistency with well-established results in the literature.

Table 2. Numerical values of $-\theta'(0)$ for distinct values of Pr at $\alpha = \lambda = \delta = \Omega_t = \Omega_b = \Upsilon = 0.0$.

Pr	Khan and Pop [42]	Present work
0.07	0.0663	0.066299808723
0.20	0.1691	0.169071098740
0.70	0.4539	0.453870145925
2.00	0.9113	0.911288014789
7.00	1.8954	1.895399501478

6. Results and discussion

This study examines the influence of key governing parameters on fluid flow, heat transfer, and mass transport through advanced numerical modeling. The analysis begins by transforming the original governing equations into a computationally tractable form using appropriate mathematical formulations. The transformed system is then solved numerically using an innovative merged Fibonacci-Lucas polynomial approach, which provides high-accuracy solutions for the nonlinear coupled equations. The computational implementation leverages MATHEMATICA's robust symbolic and numerical capabilities to generate comprehensive solutions for the velocity, temperature, and concentration fields. From these fundamental distributions, derived physical quantities, including surface shear stress (skin friction coefficient) and rates of heat and mass transfer (Nusselt and Sherwood numbers), are calculated through systematic differentiation and post-processing of the primary solution variables. This approach enables precise characterization of the transport phenomena while maintaining numerical stability across the parameter space. As shown in Figure 2, the variable density parameter δ significantly influences the velocity $f'(\eta)$, temperature $\theta(\eta)$, and concentration $\phi(\eta)$ profiles. An increase in δ makes the fluid's density more responsive to temperature changes, leading to noticeable shifts in flow behavior. This is because a higher δ strengthens the density gradient in the boundary layer, thereby modifying momentum distribution. The resulting increased resistance to fluid motion causes a reduction in the velocity, temperature, and concentration profiles. Therefore, the variable density parameter is vital in controlling the energy and mass transport properties of the nanofluid system. Physically, increasing the variable density parameter enhances the density gradient, which strengthens resistance to flow and reduces the velocity, temperature, and concentration profiles.

The Williamson parameter λ characterizes the non-Newtonian pseudoplastic behavior of the fluid, where increasing λ signifies stronger deviation from Newtonian viscosity. As evidenced in Figure 3, increasing λ significantly alters the transport dynamics: the velocity profile $f'(\eta)$ diminishes near the surface due to enhanced shear-thinning effects, which reduce the fluid's resistance to deformation and weaken convective momentum transfer. Concurrently, the temperature profile $\theta(\eta)$ rises away from the sheet, indicating a shift toward diffusion-dominated heat transfer as convective transport becomes less effective. The concentration field $\phi(\eta)$ also responds to these changes, exhibiting a

gradual enhancement with higher λ values, likely due to the combined effects of suppressed momentum diffusion and sustained nanoparticle mobility under shear-thinning conditions. The observed patterns illustrate how the Williamson parameter adjusts the equilibrium among viscous, thermal, and mass transport mechanisms. This has significant implications for optimizing non-Newtonian nanofluid systems in scenarios where precise heat and mass transfer performance is essential. Physically, increasing the Williamson parameter enhances shear-thinning, which reduces near-surface velocity while promoting diffusion-dominated heat and mass transfer.

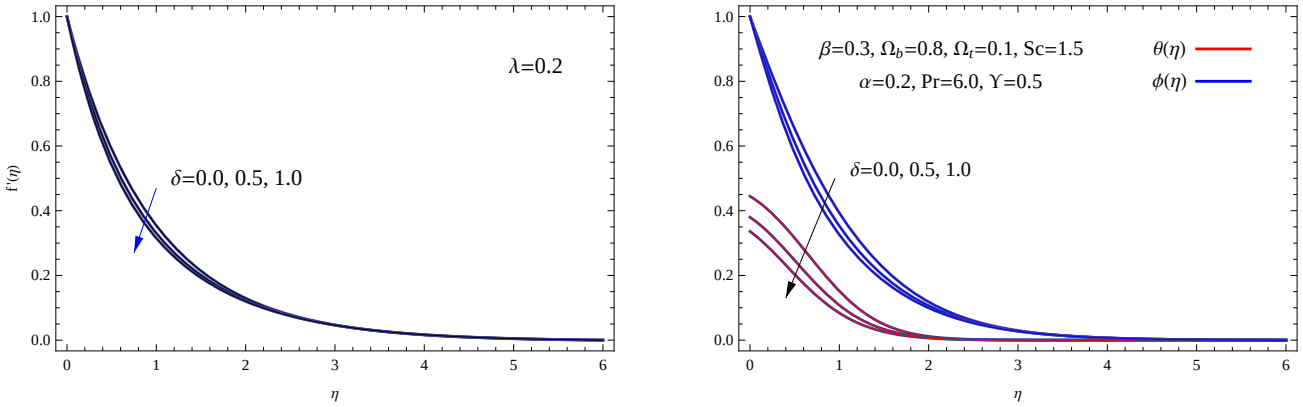

Figure 2. Variation of δ on $f'(\eta)$, and variation of δ on $\phi(\eta)$ and $\theta(\eta)$.

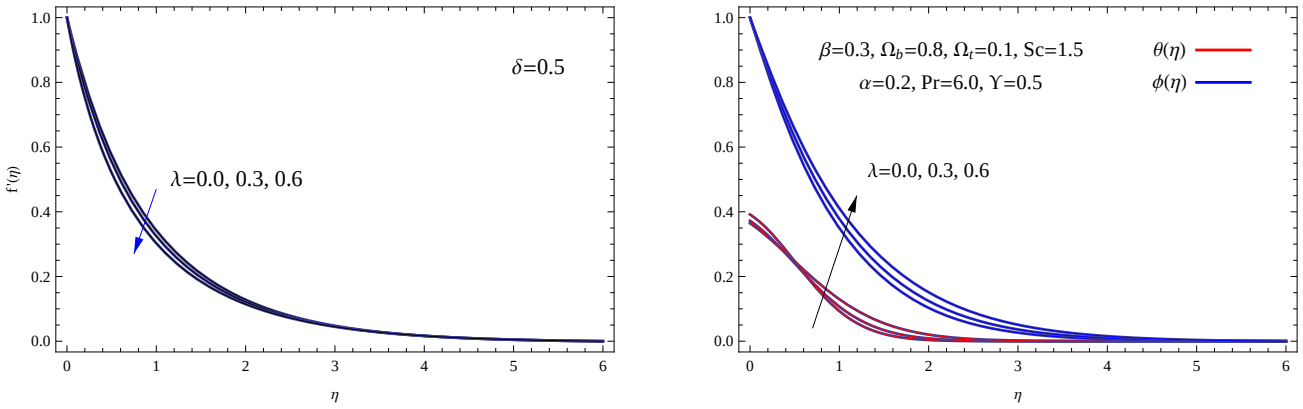

Figure 3. Variation of λ on $f'(\eta)$, and variation of λ on $\phi(\eta)$ and $\theta(\eta)$.

As demonstrated in Figure 4, both the radiation parameter Υ and convection parameter β critically modify the thermal characteristics $\theta(\eta)$ of the boundary layer. The radiation effect shows a direct correlation with temperature distribution, where elevated Υ values substantially strengthen radiative heat flux within the fluid medium, producing a marked temperature increase, particularly in regions distant from the stretching surface. This thermal enhancement occurs because radiation provides supplementary energy input, effectively expanding the thermal boundary layer thickness while raising the overall temperature magnitudes [43]. Similarly, the convection parameter β exhibits more

complex behavior. Increased β values amplify surface heat transfer rates to the ambient medium, yet lead to higher temperature fields within the boundary layer. This apparent behavior stems from the parameter's role in governing the convective boundary condition, in which stronger convective coupling actually reduces cooling efficiency at the surface-to-fluid interface, thereby promoting thermal energy accumulation in the near-wall region. Physically, increasing the radiation and convection parameters enhances thermal energy within the boundary layer by boosting radiative flux and modifying surface heat exchange, leading to higher fluid temperatures.

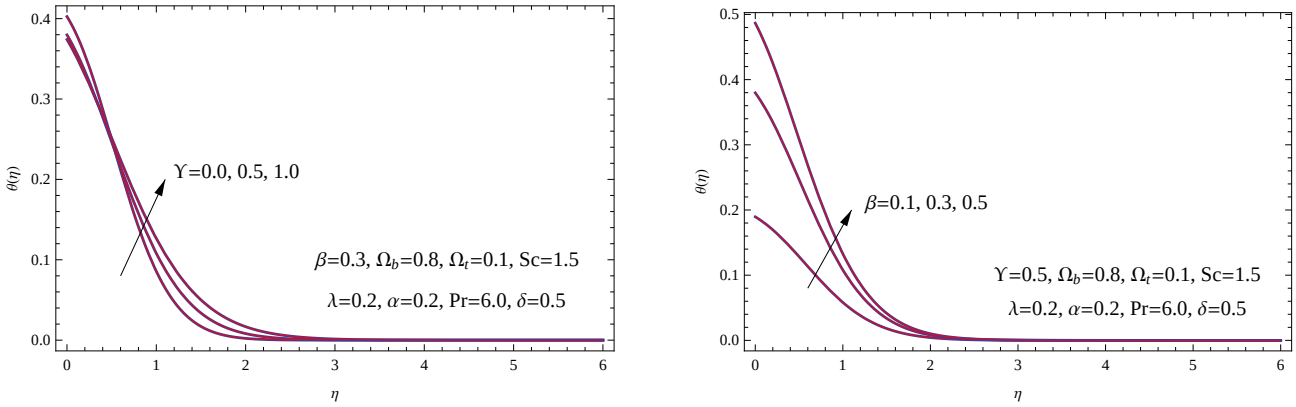

Figure 4. Variation of Υ on $\theta(\eta)$, and variation of β on $\theta(\eta)$.

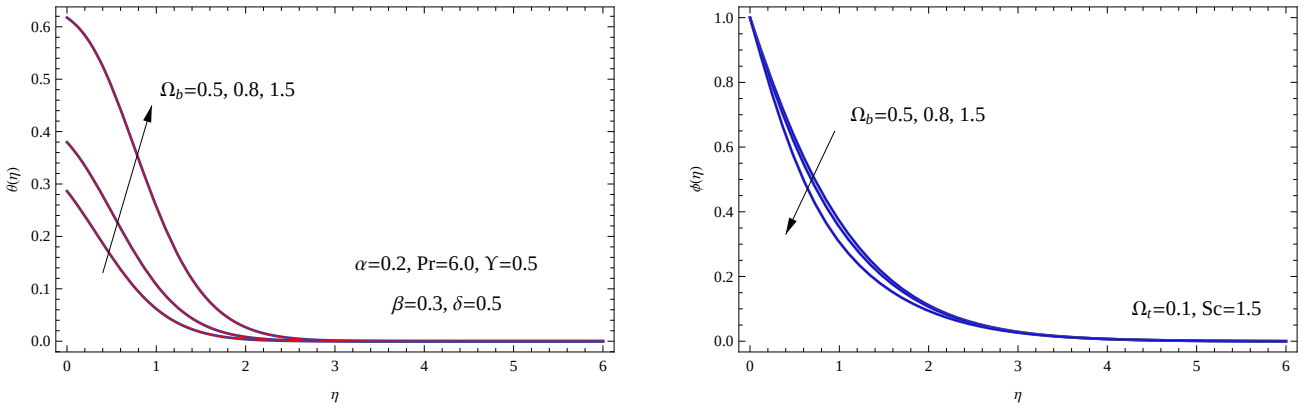

Figure 5. Variation of Ω_b on $\theta(\eta)$, and variation of Ω_b on $\phi(\eta)$.

As illustrated in Figure 5, the Brownian motion parameter Ω_b plays a role in shaping both the temperature profile $\theta(\eta)$ and the concentration profile $\phi(\eta)$. As Ω_b moves from the value 0.5 to 1.5, the temperature profile $\theta(\eta)$ rises, indicating enhanced heat transfer due to intensified particle motion and micro-scale interactions. Conversely, the concentration profile $\phi(\eta)$ decreases with higher Ω_b, as stronger Brownian diffusion promotes wider particle dispersion, reducing local concentration. These trends highlight the significant role of Brownian motion in governing heat and mass transfer dynamics in the studied system. In shaping these profiles $\theta(\eta)$ and $\phi(\eta)$, other fixed values of governing

parameters come into play: $\alpha = 0.2$, $Pr = 6.0$, $\Upsilon = 0.5$, $\beta = 0.3$, and $\delta = 0.5$. Furthermore, $Sc = 1.5$ has an effect on mass diffusion. Physically, increasing the Brownian motion parameter intensifies particle movement, which enhances heat transfer while reducing local nanoparticle concentration due to wider dispersion.

The thermophoresis parameter Ω_t significantly influences both the temperature distribution $\theta(\eta)$ and concentration profile $\phi(\eta)$ as observed from Figure 6. The temperature profile $\theta(\eta)$ increases with rising Ω_t, a phenomenon attributed to the migration of particles from hot to cold regions, which in turn enhances thermal energy transfer. Similarly, elevated Ω_t values drive particles toward cooler regions, resulting in a higher concentration distribution $\phi(\eta)$. This phenomenon illustrates thermophoresis' ability to regulate both thermal and mass transfer in nanofluidic environments. The interaction between thermophoresis and Brownian motion (Ω_b) becomes especially significant, as their combined effects govern the system's overall transport behavior.

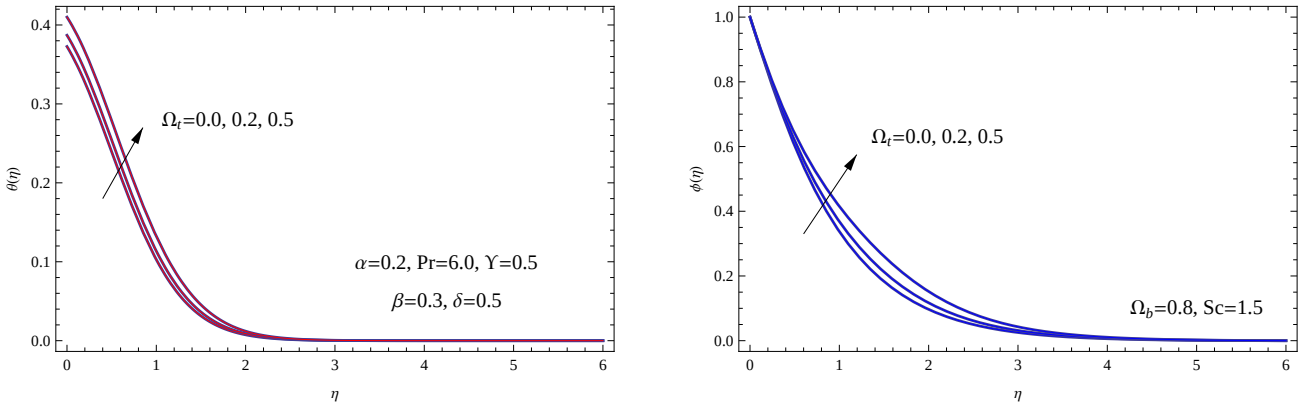

Figure 6. Variation of Ω_t on $\theta(\eta)$, and variation of Ω_t on $\phi(\eta)$.

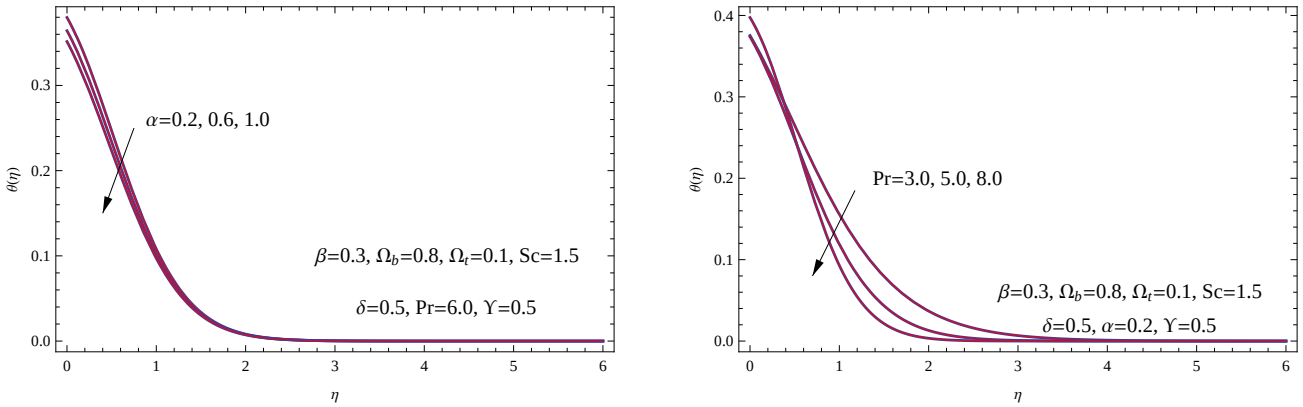

Figure 7. Variation of α on $\theta(\eta)$, and variation of Pr on $\theta(\eta)$.

Figure 7 demonstrates the significant influence of the thermal conductivity parameter α and Prandtl number Pr on the temperature distribution $\theta(\eta)$. When α rises from 0.2 to 1.0, and the Prandtl number

Pr enhances from 3.0 to 8.0, the temperature profile $\theta(\eta)$ drops, which suggests that better thermal conductivity helps heat dissipate more effectively and lessens thermal gradients. Similarly, a rise in the Prandtl number from 3.0 to 8.0 results in a clear reduction in temperature distribution. The reason for this is that fluids characterized by larger Prandtl numbers exhibit diminished thermal diffusivity, thereby hindering heat conduction and causing the thermal boundary layer to become narrower. Physically, increasing thermal conductivity and the Prandtl number enhances heat dissipation, reducing the temperature profile and narrowing the thermal boundary layer.

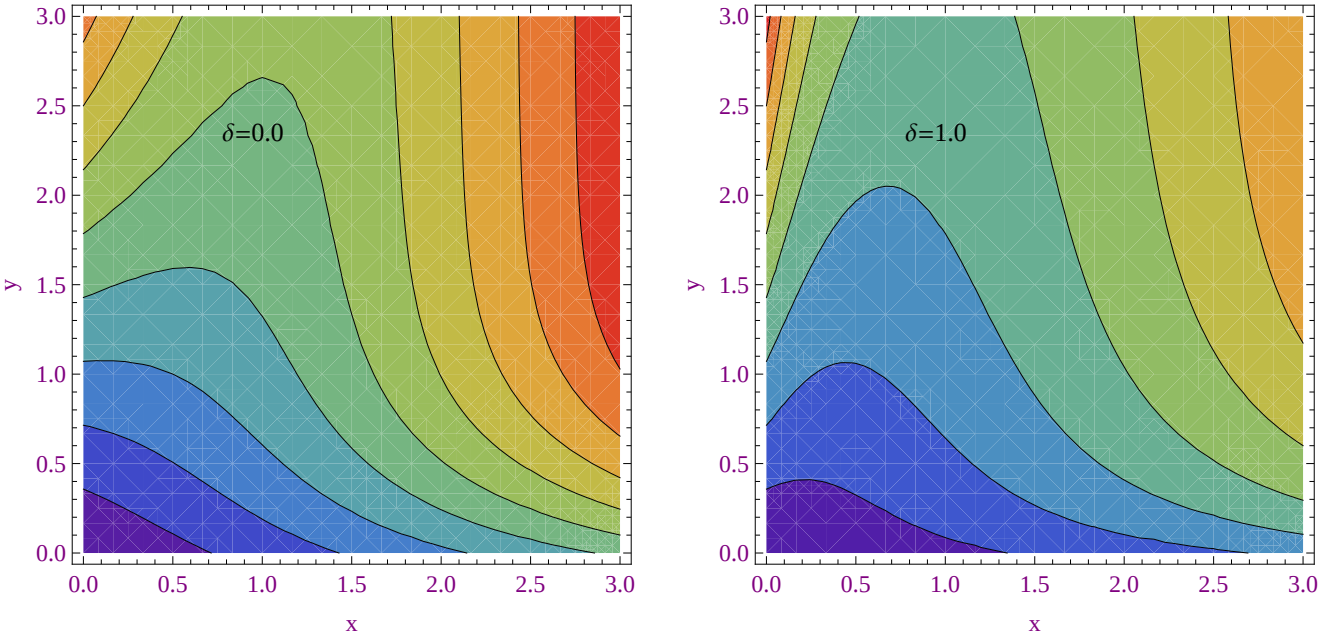

Figure 8. Stream lines for $\delta = 0.0$, and stream lines for $\delta = 1.0$.

The streamline distributions in Figure 8 demonstrate a fundamental transformation driven by the density variation parameter δ. For the case of constant density ($\delta = 0.0$), the streamlines maintain wide, uniform spacing with gentle curvature, reflecting a stable, well-developed flow field characteristic of fluids with homogeneous properties. When density variation is introduced ($\delta = 1.0$), the streamline pattern undergoes significant reorganization: the paths become more densely clustered near the surface and exhibit substantially increased curvature. This contraction occurs because the density gradient creates localized buoyancy effects that accelerate fluid elements in specific regions, thereby compressing the streamlines and intensifying the velocity gradients.

With the parameters examined, we will now investigate their impact on the skin friction coefficient $\frac{1}{2}Cf_xRe^{\frac{1}{2}}$, the local Nusselt number $Nu_xRe^{\frac{-1}{2}}$, and the local Sherwood number $Sh_xRe^{\frac{-1}{2}}$ using the data presented in Table 3. Clearly, the numerical results demonstrate significant parametric influences on surface friction $\frac{1}{2}Cf_xRe^{\frac{1}{2}}$, heat transfer $Nu_xRe^{\frac{-1}{2}}$, and mass transfer $Sh_xRe^{\frac{-1}{2}}$ characteristics. The density parameter δ shows a positive correlation with all three transport metrics-increasing δ from 0.0 to 1.0 enhances skin friction by 23.5%, the Nusselt number by 17.9%, and the Sherwood number by 33.3%. This stems from density-driven buoyancy effects that intensify near-wall gradients. Thermal

radiation factor Υ demonstrates particularly strong impact on the heat transfer mechanism, with the Nusselt number increasing 101% as Υ rises from 0.0 to 1.0, while causing only a marginal decrease in skin friction (1.1%) and the Sherwood number (1.1%) reduction.

Table 3. Values of $\frac{1}{2}Cf_xRe^{\frac{1}{2}}$, $Nu_xRe^{\frac{-1}{2}}$, and $Sh_xRe^{\frac{-1}{2}}$ after affecting with the governing parameters with $S_c = 1.5$.

δ	λ	Υ	β	Ω_b	Ω_t	α	Pr	$\frac{1}{2}Cf_xRe^{\frac{1}{2}}$	$Nu_xRe^{\frac{-1}{2}}$	$Sh_xRe^{\frac{-1}{2}}$
0.0	0.2	0.5	0.3	0.8	0.1	0.2	6.0	0.96084	0.264725	0.743891
0.5	0.2	0.5	0.3	0.8	0.1	0.2	6.0	1.08169	0.293251	0.874339
1.0	0.2	0.5	0.3	0.8	0.1	0.2	6.0	1.18692	0.312212	0.991787
0.5	0.0	0.5	0.3	0.8	0.1	0.2	6.0	1.12885	0.288031	0.889139
0.5	0.3	0.5	0.3	0.8	0.1	0.2	6.0	1.05574	0.296551	0.825623
0.5	0.6	0.5	0.3	0.8	0.1	0.2	6.0	0.96097	0.299807	0.759778
0.5	0.2	0.0	0.3	0.8	0.1	0.2	6.0	1.09072	0.193665	0.882749
0.5	0.2	0.5	0.3	0.8	0.1	0.2	6.0	1.08169	0.293251	0.874339
0.5	0.2	1.0	0.3	0.8	0.1	0.2	6.0	1.07863	0.389661	0.873315
0.5	0.2	0.5	0.1	0.8	0.1	0.2	6.0	1.01907	0.124643	0.810557
0.5	0.2	0.5	0.3	0.8	0.1	0.2	6.0	1.08169	0.293251	0.874339
0.5	0.2	0.5	0.5	0.8	0.1	0.2	6.0	1.11885	0.410001	0.911943
0.5	0.2	0.5	0.3	0.5	0.1	0.2	6.0	1.05435	0.333374	0.823646
0.5	0.2	0.5	0.3	0.8	0.1	0.2	6.0	1.08169	0.293251	0.874339
0.5	0.2	0.5	0.3	1.5	0.1	0.2	6.0	1.15117	0.186324	0.991819
0.5	0.2	0.5	0.3	0.8	0.0	0.2	6.0	1.07973	0.296309	0.880979
0.5	0.2	0.5	0.3	0.8	0.2	0.2	6.0	1.08371	0.290094	0.868497
0.5	0.2	0.5	0.3	0.8	0.5	0.2	6.0	1.09009	0.280025	0.855887
0.5	0.2	0.5	0.3	0.8	0.1	0.2	6.0	1.08169	0.293251	0.874339
0.5	0.2	0.5	0.3	0.8	0.1	0.6	6.0	1.07696	0.327797	0.867332
0.5	0.2	0.5	0.3	0.8	0.1	1.0	6.0	1.07310	0.360215	0.861648
0.5	0.2	0.5	0.3	0.8	0.1	0.2	3.0	1.07728	0.295163	0.876743
0.5	0.2	0.5	0.3	0.8	0.1	0.2	5.0	1.07906	0.295821	0.872644
0.5	0.2	0.5	0.3	0.8	0.1	0.2	8.0	1.08055	0.296505	0.870971

The convection parameter β shows similar trends, with 229% Nusselt number enhancement and 12.5% skin friction increase at higher β values, indicating strengthened thermal boundary layer development. The Williamson parameter λ exhibits an inverse relationship with both $\frac{1}{2}Cf_xRe^{\frac{1}{2}}$ and $Sh_xRe^{\frac{-1}{2}}$ but a direct correlation with the thermal transfer coefficient. As λ increases from 0.0 to 0.6, friction decreases by 14.9%, the Sherwood number reduces by 14.6%, while the Nusselt number shows modest 4.1% improvement, reflecting the competing effects of shear-thinning and viscoelastic behavior. Likewise, nanoparticle transport parameters reveal contrasting behavior, where Brownian motion parameter Ω_b enhances mass transfer by approximately 20.4% while reducing heat transfer by approximately 44.1%, whereas thermophoresis Ω_t shows inverse effects in the thermal transfer mechanism and a positive impact in the mass transfer mechanism. Additionally, the conductivity

parameter α improves the Nusselt number by 22.8% with minimal impact on other quantities.

7. Conclusions

This study successfully developed and analyzed a comprehensive model for non-Newtonian Williamson nanofluid flow over an impermeable stretching surface. The framework incorporated temperature-dependent density, thermal conductivity, mixed convection, nanoparticle dynamics, and thermal radiation effects. The numerical methodology, combining Fibonacci-Lucas polynomials with least squares approximation, demonstrated remarkable accuracy and stability. Results confirm the approach's effectiveness in capturing crucial physical phenomena, establishing a reliable foundation for investigating thermally sensitive fluids with complex rheological behavior. Key findings reveal that:

(1) The density and convection parameters notably boost all transport rates, leading to substantial increases in skin friction, heat transfer, and mass transfer.
(2) The Williamson parameter and Brownian motion exhibit contrasting effects: while they reduce friction and thermal transfer, they simultaneously enhance mass transport.
(3) Heat transfer performance is considerably enhanced by thermal radiation and conductivity, evidenced by radiation's over 100% increase in the Nusselt number, highlighting their key role in thermal energy movement.
(4) Increasing the variable density parameter decreases the velocity, temperature, and concentration profiles, underscoring its significant impact on flow and transport characteristics.
(5) The thermophoresis effect significantly improves temperature and concentration profiles, demonstrating its critical influence on regulating energy and particle transfer in nanofluid applications.
(6) Future work may extend the present spectral framework to unsteady or three-dimensional Williamson nanofluid flows, enabling broader application to advanced thermal management systems.

Author contributions

M. M. Khader: Investigation, Conceptualization, Formal analysis, Software, Original draft preparation, Writing-review and editing; M. Adel: Writing-Original draft preparation, Methodology, Supervision, Formal analysis, Visualization, Writing; M. M. Babatin: Writing-review and editing, Original draft preparation, Methodology, Software, Investigation; A. Alaidrous: Formal analysis, Software, Methodology, Writing-review and editing.

Use of Generative-AI tools declaration

The authors declare they have not used Artificial Intelligence (AI) tools in the creation of this article.

Availability of data and materials

The datasets generated during the current study are available from the corresponding author upon reasonable request.

Acknowledgements

The author (A. Alaidrous) would like to thank the Scientific Council of Umm Al-Qura University for the financial support for this research project as an academic sabbatical leave project (Accept ID 2502006443 in 28/7/2025). She also extends her sincere thanks to Umm Al-Qura University.

Conflict of interest

The authors declared that they have no conflict of interest.

References

1. S. U. S. Choi, Enhancing thermal conductivity of fluid with nanoparticles, *ASME FED*, **231** (1995), 99–105. http://doi.org/10.1115/IMECE1995-0926
2. U. Rashid, D. Baleanu, A. Iqbal, M. Abbas, Shape effect of nanosize particles on magnetohydrodynamic nanofluid flow and heat transfer over a stretching sheet with entropy generation, *Entropy*, **22** (2020), 1171. http://doi.org/10.3390/e22101171
3. E. Alali, A. M. Megahed, MHD dissipative Casson nanofluid liquid film flow due to an unsteady stretching sheet with radiation influence and slip velocity phenomenon, *Nanotechnol. Rev.*, **11** (2022), 463–472. http://doi.org/10.1515/ntrev-2022-0031
4. W. Abbas, M. A. Ibrahim, O. Mokhtar, A. M. Megahed, A. A. M. Said, Numerical analysis of MHD nanofluid flow characteristics with heat and mass transfer over a vertical cone subjected to thermal radiation and chemical reaction, *J. Nonlinear Math. Phys.*, **30** (2023), 1540–1566. http://doi.org/10.1007/s44198-023-00142-4
5. M. Garvandha, N. Gajjeia, V. Naria, D. Kumar, Thermodynamic entropy of a magnetized nanofluid flow over an inclined stretching cylindrical surface, *J. Therm. Eng.*, **10** (2024), 1253–1265. http://dx.doi.org/10.14744/thermal.0000865
6. A. M. Amer, Nourhan I. Ghoneim, A. M. Megahed, Investigation of dissipation phenomenon of non-Newtonian nanofluid due to a horizontal stretching rough sheet through a Darcy porous medium, *Appl. Eng. Sci.*, **17** (2024), 100171. http://doi.org/10.1016/j.apples.2023.100171
7. L. Ali, R. Apsari, A. Abbas, P. Tak, Entropy generation on the dynamics of volume fraction of nanoparticles and Coriolis force impacts on mixed convective nanofluid flow with significant magnetic effect, *Numer. Heat Trans.r, Part A: Appl.*, **86** (2025), 8509–8524. http://doi.org/10.1080/10407782.2024.2360652
8. A. Mishra, G. Pathak, Thermal-flow characteristics of an Ellis hybrid nanofluid containing polytetrafluoroethylene-SWCNTs over a stretching/shrinking cylinder with slip effect, *Nano-Struct. Nano-Objects*, **43** (2025), 101515. http://doi.org/10.1016/j.nanoso.2025.101515

9. A. Mishra, Analysis of radiative Ellis hybrid nanofluid flow over a stretching/shrinking cylinder embedded in a porous medium with slip condition, *Multiscale Multi. Mod.*, **8** (2025), 282. http://doi.org/10.1007/s41939-025-00871-7
10. M. A. A. Hamad, M. J. Uddin, A. M. Ismail, Radiation effects on heat and mass transfer in MHD stagnation-point flow over a permeable flat plate with convective boundary condition, *Nucl. Eng. Des.*, **242** (2012), 194–200. http://doi.org/10.1016/j.nucengdes.2011.09.005
11. M. M. Khader, A. M. Megahed, Differential transformation method for flow and heat transfer due to a stretching sheet embedded in a porous medium, *Appl. Math. Mech.*, **35** (2014), 1387–1400. http://doi.org/10.1007/s10483-014-1870-7
12. A. Hamid, M. Khan, Unsteady mixed convective flow of Williamson nanofluid in the presence of variable thermal conductivity and magnetic field, *J. Mol. Liq.*, **260** (2018), 436–446. http://doi.org/10.1016/j.molliq.2018.03.079
13. S. U. Jan, U. Khan, M. Abd El-Rahman, S. Islam, A. M. Hassan, A. Ullah, Effect of variable thermal conductivity of ternary hybrid nanofluids over a stretching sheet with convective boundary conditions and magnetic field, *Results Eng.*, **20** (2023), 101531. http://doi.org/10.1016/j.rineng.2023.101531
14. T. S. Khaleque, A. Hossain, M. D. Shamshuddin, M. Ferdows, S. O. Salawu, S. Sun, Soret and Dufour impacts on radiative power-law fluid flow via a continuously stretchable surface with varying viscosity and thermal conductivity, *Sci. Rep.*, **14** (2024), 23152. http://doi.org/10.1038/s41598-024-73426-4
15. A. M. Salem, M. Abd El-Aziz, E. M. Abo-Eldahab, I. Abd-Elfatah, Effect of variable density on hydromagnetic mixed convection flow of non-Newtonian fluid, *Commun Nonlinear Sci. Numer. Simul.*, **15** (2010), 1485–1493. http://doi.org/10.1016/j.cnsns.2009.06.005
16. S. Siddiqa, S. Asghar, M. A. Hossain, Radiation effects in mixed convection flow with temperature-dependent density, *J. Eng. Phys. Thermophys.*, **85** (2012), 339–348. http://doi.org/10.1007/s10891-012-0658-1
17. S. Siddiqa, M. A. Hossain, R. S. R. Gorla, Temperature-dependent density effects on natural convection flow over a horizontal circular disk, *J. Thermophys. Heat Trans.*, **30** (2016), 890–896. http://doi.org/10.2514/1.T4941
18. Z. Ullah, N. Jabeen, M. U. Khan, Oscillatory heat transfer and current density along a nonconducting cylinder with reduced gravity and stratification, *Mathematics*, **11** (2023), 21–34. http://doi.org/10.3390/math11092134
19. Z. Ullah, A. Hussain, M. S. Aldhabani, N. H. Altaweel, S. Shahab, Temperature-dependent density on dissipative and reactive nanofluid flows, *Lubricants*, **11** (2023), 410. http://doi.org/10.3390/lubricants11090410
20. I. Boukholda, Z. Ullah, Y. M. Mahrous, A. Alamer, M. B. Amara, M. D. Alsulami, et al., Thermal density and heat sink effects in dissipative nanofluid over a magnetized sheet, *Case Stud. Therm. Eng.*, **55** (2024), 104185. http://doi.org/10.1016/j.csite.2024.104185

21. I. Haider, J. Younis, N. Jabeen, A. Hussain, I. A. Shaaban, M. A. Mohsin, M. A. Assiri, Viscous dissipation and variable density impact on heat-mass transmission in magneto Ree-Eyring nanofluid across stretched sheet, *Case Stud. Therm. Eng.*, **68** (2025), 105871. http://doi.org/10.1016/j.csite.2025.105871

22. M. A. Fahmy, A new LRBFCM-GBEM modeling algorithm for general solution of time fractional-order dual phase lag bioheat transfer problems in functionally graded tissues, *Numer. Heat Trans., Part A: Appl.*, **75** (2019), 616–626. http://doi.org/10.1080/10407782.2019.1608770

23. M. A. Fahmy, A. Almutlg, Boundary element method solution of a fractional bioheat equation for memory-driven heat transfer in biological tissues, *Fractal Fract.*, **9** (2025), 565. http://doi.org/10.3390/fractalfract9090565

24. W. M. Abd-Elhameed, H. M. Ahmed, A. Napoli, V. Kowalenko, New formulas involving Fibonacci and certain orthogonal polynomials, *Symmetry*, **15** (2023), 736. http://doi.org/10.3390/sym15030736

25. W. M. Abd-Elhameed, A. F. Abu-Sunayh, M. H. Alharbi, A. G. Atta, Spectral tau technique via Lucas polynomials for the time-fractional diffusion equation, *AIMS Mathematics*, **9** (2024), 34567–34587. http://doi.org/10.3934/math.20241646

26. Z. Wu, W. Zhang, Several identities involving Fibonacci polynomials and Lucas polynomials, *J. Inequa. Appl.*, **2013** (2013), 205. http://doi.org/10.1186/1029-242X-2013-205

27. W. M. Abd-Elhameed, A. N. Philippou, N. A. Zeyada, Novel results for generalized Fibonacci and Lucas polynomials, *Mathematics*, **10** (2022), 23–42. http://doi.org/10.3390/math10132342

28. N. Yilmaz, I. Aktas, Special transforms of generalized bivariate Fibonacci and Lucas polynomials, *Hacettepe J. Math. Stat.*, **52** (2023), 640–651. http://dergipark.org.tr/en/download/article-file/2402660

29. W. M. Abd-Elhameed, N. A. Zeyada, New formulas involving k-Fibonacci and k-Lucas polynomials, *Ind. J. Pure Appl. Math.*, **53** (2022), 1006–1016. http://doi.org/10.1007/s13226-021-00214-5

30. A. Nalli, P. Haukkanen, On generalized Fibonacci and Lucas polynomials, *Chaos, Solitons Fractals*, **42** (2009), 3179–3186. http://doi.org/10.1016/j.chaos.2009.04.048

31. S. Haq, I. Ali, Approximate solution of two-dimensional Sobolev equation using Lucas and Fibonacci polynomials, *Eng. Comput.*, **38** (2022), 2059–2068. http://doi.org/10.1007/s00366-021-01327-5

32. S. Sabermahani, Y. Ordokhani, P. Rahimkhani, Application of generalized Lucas wavelet method for nonlinear fractal-fractional optimal control problems, *Chaos, Soliton. Fract.*, **170** (2023), 113348. http://doi.org/10.1016/j.chaos.2023.113348

33. M. M. Khader, M. Adel, Investigation of Reiner-Philippoff nanofluid flow over a stretching sheet considering diffusion and first-order velocity slip: Numerical and theoretical analysis, *ZAMM*, **105** (2025), e70245. http://doi.org/10.1002/zamm.70245

34. M. M. Khader, A. Hijaz, A. M. Megahed, Engineering applications through numerical treatment of non-Newtonian nanofluid on nonlinear stretching surface, *Case Stud. Therm. Eng.*, **51** (2023), 103641. http://doi.org/10.1016/j.csite.2023.103641

35. A. M. Megahed, M. G. Reddy, W. Abbas, Modeling of MHD fluid flow over an unsteady stretching sheet with thermal radiation, variable fluid properties and heat flux, *Math. Comput. Simul.*, **185** (2021), 583–593. https://doi.org/10.1016/j.matcom.2021.01.011

36. A. M. Megahed, Improvement of heat transfer mechanism through a Maxwell fluid over a stretching sheet, *Math. Comput. Simul.*, **187** (2021), 97–109. http://doi.org/10.1016/j.matcom.2021.02.018

37. Z. Ullah, M. M. Alam, F. E. Merga, U. Tariq, F. Albouchi, Y. M. Mahrous, et al., Variable density and heat generation impact on chemically reactive Carreau nanofluid with convective heating, *Case Stud. Therm. Eng.*, **63** (2024), 105260. http://doi.org/10.1016/j.csite.2024.105260

38. W. M. Abd-Elhameed, Novel formulas of generalized Jacobi polynomials, *Mathematics*, **10** (2022), 4237. http://doi.org/10.3390/math10224237

39. W. M. Abd-Elhameed, O. M. Alqubori, New expressions for polynomials combining Fibonacci and Lucas polynomials, *AIMS Mathematics*, **10** (2024), 2930–2957. http://doi.org/10.3934/math.2025136

40. K. Parand, M. Delkhosh, Operational matrices to solve nonlinear Volterra-Fredholm integro-differential equations, *GU. J. Sci.*, **29** (2016), 895–907.

41. S. Nadeem, S. T. Hussain, C. Lee, Flow of a Williamson fluid over a stretching sheet, *Braz. J. Chem. Eng.*, **30** (2013), 619–625. http://doi.org/10.11648/j.ijse.20210501.12

42. W. A. Khan, I. Pop, Boundary-layer flow of a nanofluid past a stretching sheet, *Int. J. Heat Mass Trans.*, **53** (2010), 2477–2483. http://doi.org/10.1016/j.ijheatmasstransfer.2010.01.032

43. L. Ali, P. Kumar, H. Poonia, S. Areekara, R. Apsari, The significant role of Darcy-Forchheimer and thermal radiation on Casson fluid flow subject to stretching surface: A case study of dusty fluid, *Modern Phys. Lett. B*, **38** (2024), 2350215. http://doi.org/10.1142/S0217984923502159

AIMS Press